

pubs.acs.org/journal/ascecg Research Article

Insights into a Nitrogen-Doped Cobalt Oxide Catalyst for Enhanced Hydrogenation of CO_2 to C_{2+} Hydrocarbons

Ming-Ming Yu, [&] Zhenghao Zhang, [&] Gui-Ling Guan, [&] Bhagyesha Patil, Priya Darshini Srinivasan, Guiru Wang, * Wen-Hua Feng, Yu-Ting Miao, Li-Jun Wang, Hongda Zhu, Mohsen Shakouri, Rong Huang, Ding Ding, Wenwu Sun, Juan J. Bravo-Suárez, * Yongfeng Hu, Si-Min Yu, Yi Cui, Qiang Wang, Jin-Hui Yang, Jian-Feng Wu, * and Lingjun Chou



Cite This: ACS Sustainable Chem. Eng. 2024, 12, 5496-5508

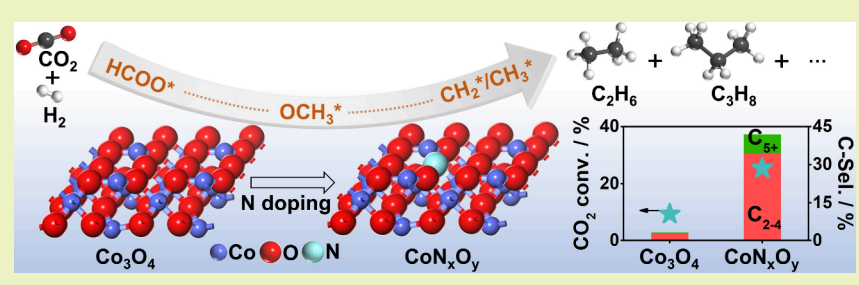


ACCESS

III Metrics & More

Article Recommendations

s Supporting Information



ABSTRACT: Hydrogenation of CO_2 to C_{2+} hydrocarbons over non-noble metal catalysts is essential from environmental and economic aspects. However, increasing the selectivity of C_{2+} hydrocarbons is still challenging for Co-based catalysts, as their predominant selectivity is toward CH_4 (>99%). Herein, this work provides insights into the mechanism of CO_2 hydrogenation over a N-doped Co_3O_4 (CoN_xO_y) catalyst with a higher CO_2 conversion (25%) and C_{2+} hydrocarbon selectivity (42 C-mol%) compared to the Co_3O_4 parent material (9% and 3 C-mol%, respectively). An increased concentration of oxygen vacancies and a decreased surface basicity strength in CoN_xO_y correlated with its enhanced catalytic performance. *In situ* diffuse reflectance infrared Fourier transform spectroscopy and density functional theory calculations revealed the evolution of reaction intermediates and the N-doping benefits on the CoN_xO_y catalyst for high activity toward C_{2+} hydrocarbons. The findings were consistent with a CO_2 hydrogenation catalytic cycle, where CO and C_{2+} hydrocarbons are mainly produced through carbonate and formate reaction pathways, respectively. Overall, we found that a relatively simple nitridation procedure can enhance the catalytic activity and selectivity of cobalt oxide toward higher hydrocarbons. This methodology could be extended to improve other transition metal-based catalysts for CO_2 conversion.

KEYWORDS: carbon dioxide, doping, Co-based catalysts, hydrogenation, reaction mechanisms

INTRODUCTION

Exploiting CO_2 as an alternative carbon source presents a unique opportunity for chemical production and the alleviation of anthropogenically emitted CO_2 .^{1–7} However, the activation and conversion of CO_2 are challenging because of CO_2 's stable thermodynamic nature.² Nevertheless, green hydrogen (H_2) , with its high intrinsic energy obtained from renewable energy sources, could be one solution to address these issues.⁴ The synthesis of high-value-added chemicals, such as light hydrocarbons (C_{2-4}) and fuels through CO_2 hydrogenation, is essential from both environmental and economic perspectives. Recently, considerable progress has been made in designing catalysts to activate and transform CO_2 .^{5–7} but selectivity control toward C_{2+} hydrocarbons instead of methane remains a great challenge.^{8–11}

Decades of experience^{12–15} obtained from Fischer–Tropsch synthesis (FTS, using CO and H₂ as a feedstock) have been

instructive for designing catalysts for CO_2 hydrogenation toward C_{2+} hydrocarbons. The FTS metal components, based on Ru, Fe, and Co elements, have high activity in synthesizing C_{2+} hydrocarbons from $CO.^{12-19}$ Among these, non-noble metal catalysts have attracted considerable interest owing to their low cost and comparable activities. For example, modified Fe-based catalysts have been proven effective in producing heavy hydrocarbons from CO_2 at high temperatures through the tandem catalysis of sequential reverse water—gas shift (RWGS, $CO_2 + H_2 = CO + H_2O$) and FTS process. 20,21 This

Received: December 2, 2023 Revised: March 5, 2024 Accepted: March 6, 2024 Published: March 22, 2024





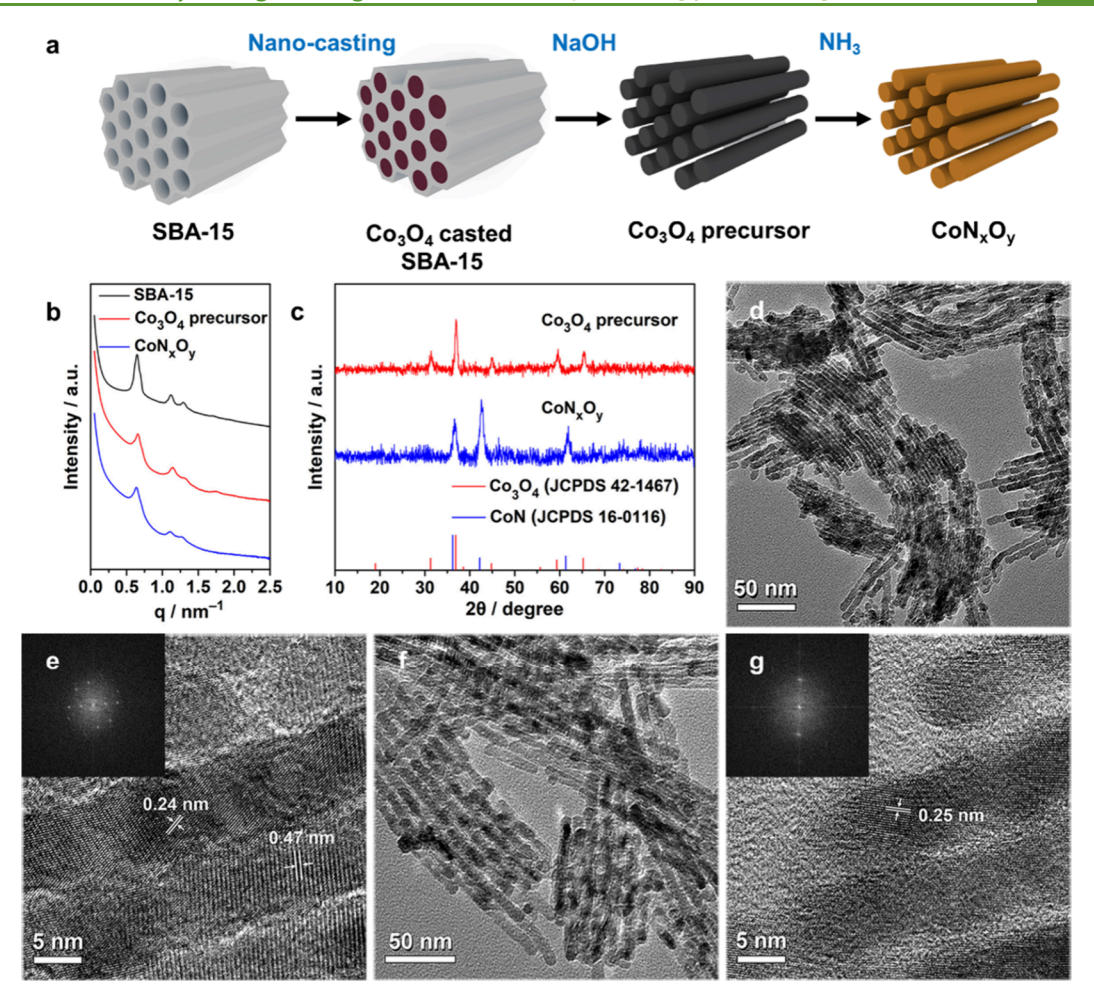


Figure 1. Characterization of mesoporous Co_3O_4 and CoN_xO_y nanowire arrays. (a) A schematic diagram for the preparation of the CoN_xO_y catalyst. (b) Small-angle X-ray scattering patterns of commercial SBA-15, the Co_3O_4 precursor, and the CoN_xO_y catalyst. (c) PXRD patterns of the Co_3O_4 precursor and CoN_xO_y catalyst. (d, e) TEM and HRTEM images of the Co_3O_4 precursor. (f, g) TEM and HRTEM images of the CoN_xO_y catalyst. The insets in panels e and g show the corresponding fast Fourier transform patterns. Note: PXRD and XPS O 1s results (*vide infra*) indicate that a CoN_xO_y phase, instead of CoN_y is formed upon the nitridation of Co_3O_4 .

is due to the high activity of the Fe_3O_4 phase 21 for the RWGS reaction and the Fe_5C_2 phase 20 for the formation of α -olefins. Unexpectedly, the selectivity toward CH_4 is high in the case of Co-based catalysts, reaching over 99% when the carbon feedstock is switched from CO to CO_2 , which may be due to the inverse adsorption behavior of CO_2 on the surface. For example, although sizable metallic cobalt nanoparticles are a good choice for conventional FTS, CO_2 -FTS mainly leads to methane because metallic Co is a poor RWGS catalyst. Alternatively, Co^{2+} on a SiO_2 support 23 and cobalt oxide on metal oxide supports 6,24 (e.g., TiO_2) could facilitate the RWGS process, resulting in improved selectivity toward CO but with minimal C-C coupling products. Therefore, suppressing the formation of CH_4 and increasing the generation of C_{2+} hydrocarbons are the primary challenges for the hydrogenation of CO_2 to produce C_{2+} hydrocarbons on Co-based catalysts.

Other catalysts, such as metal carbides, $^{17,20,25-27}$ are known to be active for C–C coupling reactions during CO hydrogenation. We surmise that transition metal nitrides, with a Pt-like electronic state for hydrogen spillover, can perform similarly in CO_2 hydrogenation. $^{28-30}$ To the best of our knowledge, no examples of cobalt nitride or N-doped cobalt oxide catalysts have been reported to hydrogenate CO_2 to C_{2+} hydrocarbons through thermal catalysis. Herein, we aim

to enhance the selectivity toward C_{2+} hydrocarbons on highly coordinated Co-based oxide surfaces by a simple nitridation process.

In this study, we synthesized uniform Co₃O₄ nanowire arrays as a precursor and the corresponding nitrided Co₃O₄ (CoN_xO_y) catalyst using a hard-templating nanocasting method. The structure and oxidation state of the CoN_xO_v catalyst were determined by complementary techniques, such as powder X-ray diffraction (PXRD), transmission electron microscopy (TEM), X-ray photoelectron spectroscopy (XPS), time-of-flight secondary ion mass spectrometry (ToF-SIMS), and X-ray absorption near-edge (XANES). The CoN_xO_y catalyst exhibited enhanced CO₂ conversion (25%) and C₂₊ product selectivity (42 C-mol%) compared to the Co₃O₄ parent material (9% and 3 C-mol%, respectively). Electron paramagnetic resonance (EPR) and carbon dioxide temperature-programmed desorption (CO2-TPD) were employed to elucidate the origin of the enhanced catalytic activity. In situ diffuse reflectance infrared Fourier transform spectroscopy (DRIFTS), modulation excitation-phase sensitive detection (ME-PSD) of DRIFTS, and density functional theory (DFT) calculations were used to shed light on the reaction mechanism for the conversion of carbonate to CO and formate to C2+ hydrocarbons. We believe that these findings and the

mechanistic understanding reported here can inspire and assist in designing the next generation of low-cost CO_2 conversion catalysts for C_{2+} hydrocarbons.

EXPERIMENTAL METHODS

Synthesis of the Mesoporous Co₃O₄ Precursor. Mesoporous cobalt oxide was synthesized using SBA-15 as a rigid template, as reported in the literature.³¹ For the typical nanocasting process (Figure 1a), 1.0 g of SBA-15 and 2.2 g of Co(NO₃)₂·6H₂O were mixed in 20 cm³ of ethanol under stirring. After evaporating the ethanol at room temperature (for 2-3 days), the obtained wine-red powder was dried in an oven at 60 °C for 4 h. Then, the dried pink solid was calcined at 350 °C in flowing air (10 cm³ min⁻¹) for 5 h with a temperature ramping rate of 1 °C min⁻¹ in a muffle furnace, resulting in a black powder. Then, another 1.8 g of Co(NO₃)₂·6H₂O was dissolved in 20 cm³ of ethanol and mixed with the obtained black powder under stirring. After the ethanol was evaporated at room temperature and dried in an oven at 60 °C for 4 h, the dried black powder was calcined at 600 °C for 5 h with a temperature ramping rate of 1 °C min⁻¹. The powder was then transferred into 100 cm³ of a 16 wt% NaOH solution under stirring for 24 h to remove the silica template. After this procedure, the solid was separated and washed with deionized H2O and ethanol three times by centrifugation. The obtained mesoporous Co₃O₄ precursor was dried in a vacuum oven at 120 °C for 8 h and then stored in an argon-protected desiccator for further use.

Synthesis of the Mesoporous CoN_xO_y Catalyst. A ceramic boat containing ca. 0.2 g of the synthesized mesoporous Co_3O_4 precursor was placed in a tube furnace (ID = 80 mm, length = 1200 mm). The air remaining in the tube furnace was purged with pure NH₃ for 30 min at room temperature to ensure that the tube was fully charged with NH₃. A typical nitridation process was carried out at 325 °C for 5 h with a temperature ramping rate of 1 °C min⁻¹ under a NH₃ flow (10 cm³ min⁻¹). Meanwhile, exhausted ammonia gas was absorbed by dilute H₂SO₄. After the nitridation process, the furnace cover was opened to allow the sample inside the tube furnace to cool down to 50 °C within about 10 min. The brown powder was quickly transferred to an Ar gas glovebox and sealed.

Catalyst Characterization. Catalyst characterization details are provided in the Supporting Information, including scanning electron microscopy (SEM), N₂ physisorption, XPS, XANES, ToF-SIMS, ¹H NMR, GC/MS, Aspen equilibrium calculations, EPR, XRD, in situ DRIFTS, in situ ME-PSD-DRIFTS, and in situ XPS results.

Catalyst Evaluation. The CO₂ hydrogenation reaction was conducted in a 50 cm³ stainless-steel autoclave (Shanghai LABE Instrument Co., Ltd.). For a typical catalytic reaction, 50 mg of powdered catalyst and a heat-resistant stirring bar (Teflon-coated, $T_{\rm max}$ = ~270 °C) were charged into the glass-lined autoclave and purged three times with a mixed gas $(H_2/CO_2/Ar = 48/48/4 \text{ on a})$ volume basis) at 1.5 MPa. After that, the autoclave was charged with the gas mixture to the desired pressure at room temperature. CO₂ hydrogenation was carried out under various reaction conditions $(210-250 \, ^{\circ}\text{C}, 1.5-5.5 \, \text{MPa initial pressure}, \, \text{H}_2/\text{CO}_2 = 0.5-2, \, \text{and}$ 3-15 h of reaction time). The gaseous and liquid products were analyzed offline by gas chromatography (GC). The gaseous product was collected in a gas sampling bag, which had been vacuumed at least three times. Then, the quantification of the gaseous products was determined with a GC 9790 plus (Fuli Instruments) equipped with a TDX-01 column (2 m × 3 mm, Lanzhou Donglilong Information Technology Co., Ltd.) connected to a thermal conductivity detector (TCD) and an HP-Plot/Q column (30 m \times 0.53 mm \times 0.50 μ m) connected to a flame ionization detector (FID). Gas and liquid products were identified by GC/MS and NMR as described in the Supporting Information. Most experiments were run at least twice to guarantee repeatability. The liquid products were collected by adding 1 mL of methylbenzene containing 0.4 μ L of cyclohexane as the internal standard. Then, the liquid products were measured with an Agilent 7890A GC equipped with HP-5 (30 m \times 0.53 mm \times 0.50

 μ m) connected to a flame ionization detector (FID). CO₂ conversion was calculated according to the following relationship:

$$X_{\text{CO}_2}(\%) = \left(1 - \frac{(A'_{\text{CO}_2}/A'_{\text{Ar}})}{(A_{\text{CO}_2}/A_{\text{Ar}})}\right) \times 100\%$$
 (1)

where $A'_{\rm CO_2}$ and $A'_{\rm Ar}$ are the peak areas of the ${\rm CO_2}$ and Ar reference gas, respectively, obtained from TCD analysis after the reaction. Similarly, $A_{\rm CO_2}$ and $A_{\rm Ar}$ are also the TCD peak areas of ${\rm CO_2}$ and Ar, respectively, obtained before the reaction.

Product selectivity was calculated according to the following relationships:

$$S_i(\text{mol\%}) = \frac{A_i \times F_i}{\sum (A_i \times F_i)} \times 100\%$$
(2)

$$S_i(\text{C-mol\%}) = \frac{m \times A_i \times F_i}{\sum (m \times A_i \times F_i)} \times 100\%$$
(3)

where A_i and F_i are the peak area and the response factor of gaseous product i, respectively, and m is the number of carbon atoms in the product molecule.

Carbon balance was calculated using the following equation:

Carbon balance(%) =
$$\frac{\sum (m \times n_i) + n_{\text{CO}} + n_{\text{CO}_2,\text{final}}}{n_{\text{CO}_2,\text{initial}}} \times 100\%$$
(4)

where n_{ν} $n_{\rm CO_2}$ $n_{\rm CO_2}$ final $n_{\rm CO_2}$ initial are the molar amounts of the hydrocarbon products, CO, CO₂ after reaction, and CO₂ in the initial reactants, respectively. The average carbon balance in this work was 92%, with a standard deviation of 3.7%. This deviation from full carbon balance closure was likely due to experimental errors in the analytical measurements.

Calculations Details. The spin-polarized calculations were performed by using the density functional theory (DFT) implemented in the Vienna Ab initio Simulation Package (VASP). The Perdew–Burke–Ernzerh (PBE) generalized gradient approximation (GGA) functional was selected to express the interacting electron exchange-correlation energy. The on-site Coulombic interaction between the Co d electrons³² was corrected using U=3.5 eV. The kinetic energy cutoff for all systems was set to 400 eV, and the cubic conventional unit cell of Co_3O_4 was optimized with a 4 × 4 × 4 k-point mesh sampling. The criteria for convergence of forces were set to 0.04 eV Å $^{-1}$, and the structures were considered optimized when all forces were below this value. The (2×2) - Co_3O_4 (111) surfaces were constructed from the optimized bulk followed by a 15 Å vacuum.

■ RESULTS AND DISCUSSION

Characterization of Mesoporous Co₃O₄ and CoN_xO_y Nanowire Arrays. We used a commercial SBA-15 sample as a hard template³¹ (Figure S1) to synthesize Co₃O₄ nanowire arrays within its mesoporous structure (Figure 1a). The ordered channels with a 2D hexagonal structure in SBA-15 provide suitable sites for developing freestanding Co₃O₄ replicas. Remarkably, the mesoporous structure of SBA-15 was replicated well in the structures of the Co₃O₄ precursor and CoN_xO_y catalyst, as evidenced by their small-angle X-ray scattering (SAXS) patterns (Figure 1b). After nitridation, the crystal phase of Co₃O₄ disappeared and was replaced by a new phase of CoN, as shown in the PXRD patterns (Figure 1c). This new phase is actually CoN_xO_y (vide infra), indicating that the N element was effectively incorporated into the structure of the Co₃O₄ precursor. The TEM images of the Co₃O₄ precursor and CoN_xO_y catalyst are illustrated in Figure 1d-g, demonstrating uniform nanowire arrays with a width of

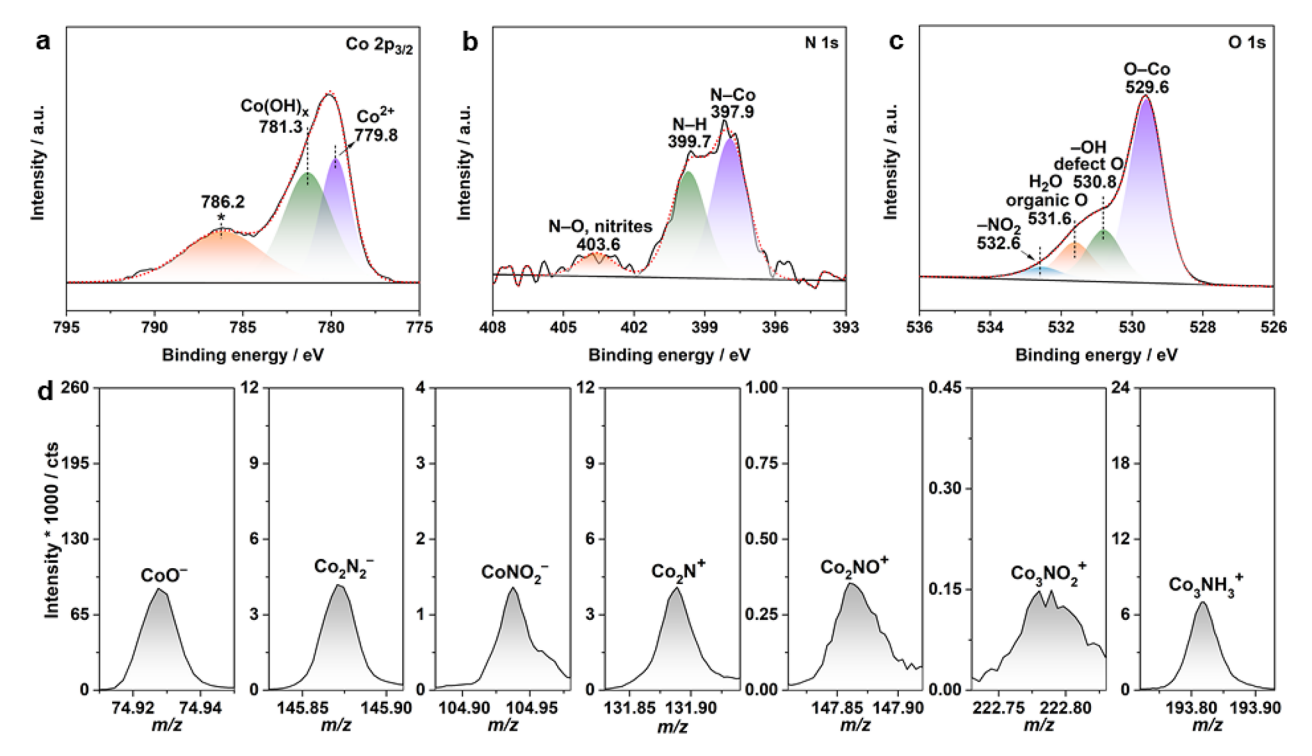


Figure 2. Structure and oxidation state of the CoN_xO_y catalyst. (a) $Co\ 2p_{3/2}$, (b) N 1s, and (c) O 1s XPS profiles of the CoN_xO_y catalyst (the black lines are the original spectra; the red lines are the fitted spectra; the purple, green, orange, and blue areas are the fitted components). (d) ToF-SIMS profiles of partially negative and positive ions derived from the CoN_xO_y catalyst. The asterisk (*) indicates the satellite peak assigned to elemental Co.

approximately 8 nm. The fast Fourier transform (FFT) patterns revealed that both the Co_3O_4 precursor and CoN_xO_y catalyst were crystalline (Figure 1e,g, insets). Additionally, elemental analysis indicated that the N content in the CoN_xO_y catalyst was approximately 1.4 wt% (Table S1). Therefore, we adopted the label " CoN_xO_y " to represent the partially nitrided Co_3O_4 catalyst. The N_2 adsorption—desorption isotherms for the Co_3O_4 precursor and CoN_xO_y catalyst (Figure S2 and Table S2) were characteristic of type-IV curves with surface areas of 95 and 91 m² g⁻¹, respectively. The observed H3 hysteresis loop and pore size distribution indicated that the pore structures were composed of flat slits and/or wedge structures,³³ which were consistent with the TEM characterization results (Figure 1d,f).

We conducted XPS measurements and ToF-SIMS analysis (Figure 2) to understand the oxidation state and structure of the CoN_xO_v catalyst. The Co $2p_{3/2}$ XPS profile of the CoN_xO_v catalyst demonstrated a strong satellite peak at 786.2 eV (Figure 2a), resembling the pattern of the CoO reference (Figure S3a) but differing from that of the Co₃O₄ precursor (Figure S3b). 34,35 This result, along with the nearly identical Co K-edge XANES for the CoNxOy catalyst and CoO reference (Figure S4), confirmed +2 as the prevalent oxidation state of Co in the CoN_xO_y catalyst.³⁶ When further combined with the ToF-SIMS results (Figure 2d), the N 1s XPS profile (Figure 2b) exhibited three peaks at 397.9, 399.7, and 403.6 eV, which were assigned to N-Co, N-H, and N-O (nitrites) structures, respectively.^{37,38} Similarly, from the XPS binding energy positions³⁹ (Figure 2c) and ToF-SIMS results (Figure 2d), the 529.6 and 532.6 eV peaks obtained from the O 1s spectrum belonged to O-Co and -NO2 species, respectively. A more in-depth analysis of the ToF-SIMS data, a technique featuring molecular specificity and surface sensitivity, 40,4

provides insights into the surface composition and structure of the CoN_xO_y catalyst. For example, the presence of selected negative and positive ions, including CoO⁻, Co₂N₂⁻, CoNO₂⁻, Co₂N⁺, Co₂NO⁺, Co₃NO₂⁺, and Co₃NH₃⁺ (Figure 2d), further indicates the existence of Co-N-Co linkages, supporting the assignments in N 1s and O 1s XPS results (Figure 2b,c). This procedure has been previously reported to prove the formation of Ga-O-Zr linkage in the GaZrO, catalyst. 42 Additionally, it has been used to demonstrate the presence of Al-O-Fe and Si-O-Fe linkages in the Fe/ZSM-5 (0.25) zeolite. 43 A proposed pictorial view of the Co-N-Co fragments in the CoN_xO_y catalyst is illustrated in Figure S5. In summary, PXRD, TEM, XPS N 1s and O 1s, and ToF-SIMS results indicate that the nitridation treatment performed in the present study led to the partial substitution of O with N in the Co₃O₄ precursor structure, resulting in the formation of the CoN_xO_v catalyst.

Catalytic Performance of CoN_xO_y . A comparative catalytic reaction was initially performed using 50 mg of the CoN_xO_y catalyst with a mixed gas of $H_2/CO_2/Ar$ in a ratio of 48/48/4 at a temperature and pressure of 240 °C and 4.5 MPa, respectively. CO, alkanes, and alkenes (C1 to C20+) were observed as products from GC, GC-MS, and ¹H NMR analyses (Figures S6-S14). Quantitative analysis confirmed that liquid products with a carbon number above 6 ($C_m \ge 6$) accounted for less than 0.61 C-mol% of the total products. Therefore, in the subsequent discussion, we only focused on products with $C_m \leq 5$ (Figures S10-S14). Additional preliminary experiments comparing the hydrogenation of CO₂ and CO on the CoN_xO_y catalyst showed a 2.6 times greater decrease in reaction pressure in the presence of CO2 compared to that in the presence of CO (Figure S15 and Table S3). Since the change in the number of moles from reactants to

products was identical in CO_2/H_2 (e.g., for alkanes: $mCO_2 + (3m+1)H_2 = C_mH_{2m+2} + 2mH_2O$, $\Delta\nu = -2m$) and CO/H_2 (e.g., for alkanes: $mCO + (2m+1)H_2 = C_mH_{2m+2} + mH_2O$, $\Delta\nu = -2m$) and the average carbon number was similar in the presence of CO_2 and CO (~2.1), the steeper pressure decay with CO_2/H_2 suggests that CO_2 hydrogenation to hydrocarbons is predominant when compared to the CO hydrogenation pathway over the CON_xO_y catalyst.

Further experiments were carried out to compare the catalytic performance among the Co_3O_4 precursor, CoO, and CoN_xO_y catalyst. As shown in Figure 3 and Table S4, the CO_2

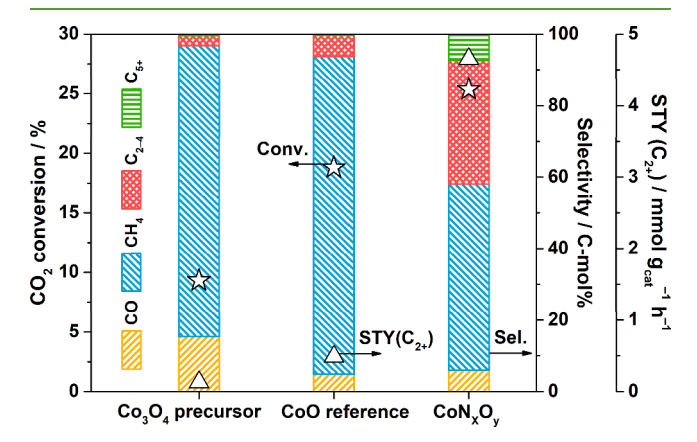


Figure 3. Comparison of the CO_2 conversion and product selectivity among the Co_3O_4 precursor, standard CoO reference, and CoN_xO_y catalyst during CO_2 hydrogenation. Reaction conditions: 50 mg of catalyst, 50 cm³ batch reactor, $H_2/CO_2/Ar = 48/48/4$, 4.5 MPa total initial pressure, 240 °C, 12 h reaction time, 350 rpm, and no solvent.

conversion and C_2 – C_4 hydrocarbon selectivity over the CoN_xO_y catalyst increased significantly by 2.7 and 12.4 times, respectively, compared to those of the Co_3O_4 precursor. Notably, after nitridation, the CO selectivity was suppressed to 6 C-mol% from 15 C-mol%, and that of methane was reduced to 52 C-mol% from 81 C-mol%. Because the initial oxidation state of Co in the CoN_xO_y catalyst was similar to that of CoO (Figure S4), we also performed catalytic tests with a standard CoO reference material. Although the standard CoO reference exhibited a high CO_2 conversion (19%), the CoN_xO_y catalyst possessed higher C_{2+} selectivity (42 C-mol%) and C_{2+} STY (5 mmol g_{cat}^{-1} h⁻¹) than the standard CoO reference (6 C-mol% and 0.5 mmol g_{cat}^{-1} h⁻¹, respectively), highlighting the positive impact of nitridation.

Next, we evaluated the catalytic performance of the CoN_xO_y catalyst at varying H_2/CO_2 mole ratios, reaction temperatures, reaction times, and reaction pressures (Figure 4). It can be seen from Figure 4a that the H_2/CO_2 mole ratio influenced the CO_2 conversion and product selectivity. For example, the CO_2 conversion and selectivity of C_{2+} hydrocarbons and CO_2 followed opposite trends. The CO_2 conversion increased with an increasing H_2/CO_2 ratio, whereas the C_{2+} hydrocarbons and the CO_3 selectivities decreased. These trends are characteristic of the complex interplay between the kinetics and equilibrium thermodynamics of the reactions involved.

When the temperature was increased to 210-250 °C ($\rm H_2/CO_2/Ar = 48/48/4$, 4.5 MPa), the CO₂ conversion gradually increased from 12% to 25% (Figure 4b). Moreover, as the temperature approached 250 °C, the selectivity for C₂₊ hydrocarbons increased from 29 C-mol% to 42–44 C-mol%, accompanied by a decrease in CO selectivity from 14 C-mol%

to 6 C-mol%. In comparison, the selectivity of CH_4 dropped from 57 C-mol% to 47 C-mol% (Figure 4b). Equilibrium calculations in this temperature range (Figure S16) show that methane is the most favorable product (>99.8%), with amounts that remain relatively steady throughout the temperature range. These results indicate that the CO_2 hydrogenation on the CoN_xO_y catalyst operates under conditions far from equilibrium.

 CO_2 conversion and product selectivity also depended on the reaction time. For example, the level of CO_2 conversion increased from 13% to 25% ($H_2/CO_2/Ar = 48/48/4$, 4.5 MPa, 240 °C) with increasing reaction time but leveled off around 12 h (Figure 4c). The selectivity for CH_4 remained relatively constant (\sim 52 C-mol%). In contrast, there was a slight decrease in CO (15 C-mol% to 6 C-mol%) with an increase in C_{2+} selectivity (33 C-mol% to 42 C-mol%).

When examining the effects of total pressure $(H_2/CO_2/Ar = 48/48/4, 1.5-5.5 \text{ MPa}, 240 °C, 12 \text{ h})$, no significant changes were observed in CO_2 conversion $(24 \pm 2\%)$ and C_{2+} hydrocarbon selectivity $(39 \pm 2 \text{ C-mol}\%)$ when the reaction pressure P increased from 1.5 to 5.5 MPa (Figure 4d). Meanwhile, the C-mole selectivity decreased for CO but increased for CO_4 , suggesting the possible presence of CO_4 0 methanation.

In summary, a comparison of the catalytic results on various cobalt-based catalysts, including a standard CoO reference, Co_3O_4 precursor, and CoN_xO_y catalyst (Figure 3, Table S5), showed that the CoN_xO_y catalyst investigated in this study has significantly enhanced selectivity for C₂₊ hydrocarbons without the need for a coadded metal promoter or support. Moreover, the CoN_xO_y catalyst was also reasonably stable in air (Figure S17). In contrast, thermodynamic equilibrium calculations (e.g., Gibbs free energy of reaction; Figure S16) indicate that methane is the most favorable product under relevant reaction conditions. The experimental parametric studies show that the CoN_xO_y catalyst produces a broad range of products, including methane (44-65 C-mol%), CO (4-15 C-mol%), C₂-C₄ (24–36 C-mol%), and C_{5+} (5–8 C-mol%) hydrocarbons. For practical purposes, the CoN_xO_y catalyst performs optimally at $P \ge 2.5$ MPa, 240 °C, a mixture of $H_2/CO_2/Ar = 48/48/4$, and a reaction time of 12 h. This results in a CO₂ conversion of 25% and C₂₊ hydrocarbon selectivity of 42 C-mol%. An aspect worth pursuing for further catalyst development is the need to strengthen the stability of the CoN_xO_y catalyst, as N loss has been observed (Figures S18 and S19). For example, after the first cycle, only 33% of the initial amount of N remained in the catalyst. Figure S18 shows that the catalytic activity of the CoN_xO_y catalyst remained after five cycles of reuse, whereas the selectivity of C2+ hydrocarbons gradually decreased in the first three cycles and then leveled off. Our speculation is that the loss of the N element may be related to the water produced during the reaction. Nevertheless, our results demonstrated that the N-doping strategy can enhance the catalytic performance of CO₂ hydrogenation catalysts toward C₂₊ hydrocarbons.

Mechanistic Insights into CO_2 Hydrogenation on the Co_3O_4 Precursor and CoN_xO_y Catalyst. Additional EPR, CO_2 -TPD, in situ XPS, and in situ infrared spectroscopy characterizations were applied to clarify the origin of the enhanced catalytic activity of the CoN_xO_y catalyst. As shown in Figure 5a, a more evident peak for the CoN_xO_y catalyst appeared at g=2.0039 in the EPR spectrum as a result of the free electrons trapped in oxygen vacancies (O_y) . The

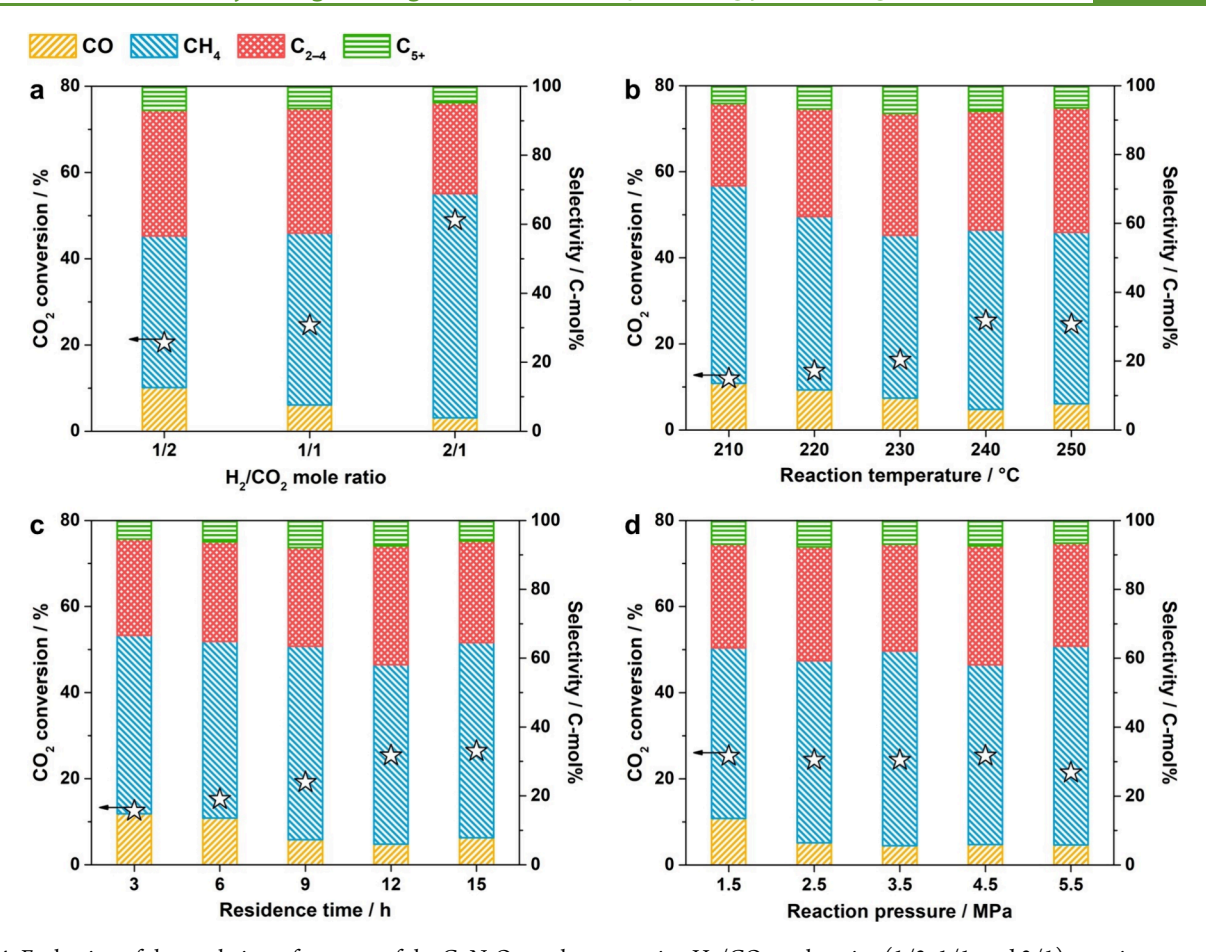


Figure 4. Evaluation of the catalytic performance of the CoN_xO_y catalyst at varying H_2/CO_2 mole ratios (1/2, 1/1, and 2/1), reaction temperatures (210–250 °C), reaction times (3–15 h), and initial total pressures (1.5–5.5 MPa). Reaction conditions: (a) 4.5 MPa of $H_2/CO_2/Ar = 32/64/4$, 48/48/4, and 64/32/4 at 250 °C for 12 h; (b) 4.5 MPa of $H_2/CO_2/Ar = 48/48/4$ at 210–250 °C for 12 h; (c) 4.5 MPa of $H_2/CO_2/Ar = 48/48/4$ at 240 °C for 3–15 h; and (d) 1.5–5.5 MPa of $H_2/CO_2/Ar = 48/48/4$ at 240 °C for 12 h. Other reaction conditions were as follows: 50 mg of catalyst, 50 cm³ of batch reactor, 350 rpm, and no solvent.

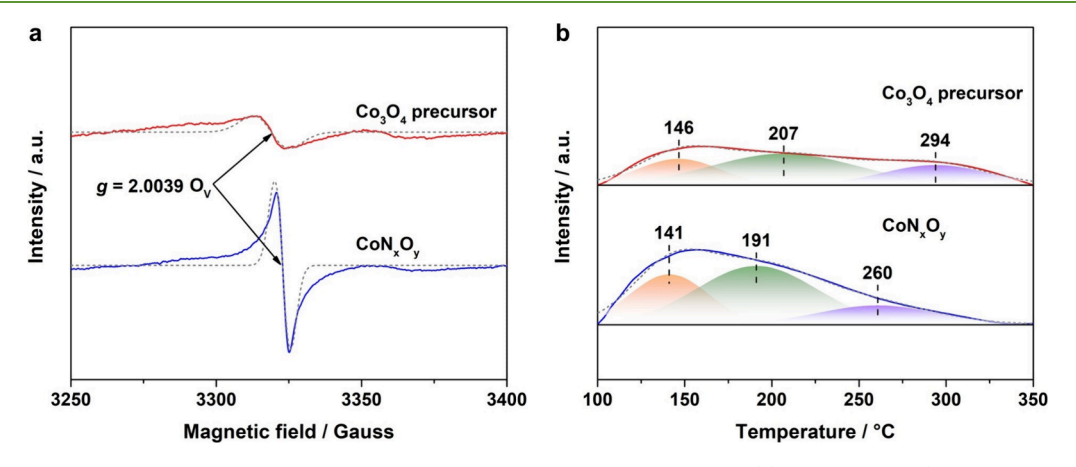


Figure 5. EPR spectra and CO_2 -TPD results of the Co_3O_4 precursor and CoN_xO_y catalyst. (a) Experimental (solid red and blue lines) and simulated (dashed gray lines) EPR spectra of the Co_3O_4 precursor and CoN_xO_y catalyst. (b) CO_2 -TPD results for the Co_3O_4 precursor and CoN_xO_y catalyst. Solid red and blue lines are the experimental results, and the dashed gray lines are the fitted TCD traces. The purple, green, and orange areas are the fitted components.

measurement of the oxygen vacancy population on the Co_3O_4 precursor and CoN_xO_y catalyst is displayed in Figure S20 and Table S6. These results indicate that the nitridation process induces the formation of a higher density of O_V in the CoN_xO_y catalyst. Figure Sb presents the CO_2 -TPD results for the Co_3O_4 precursor and the CoN_xO_y catalyst. Significant changes

were observed; for example, the Co_3O_4 precursor exhibited a more even and less intense desorption profile than the CoN_xO_y sample. This CO_2 -TPD trace was further deconvoluted into three peaks centered at approximately 146, 207, and 294 °C, which were attributed to basic sites with increasing adsorption strength. In contrast, the TPD curve for the CoN_xO_y catalyst

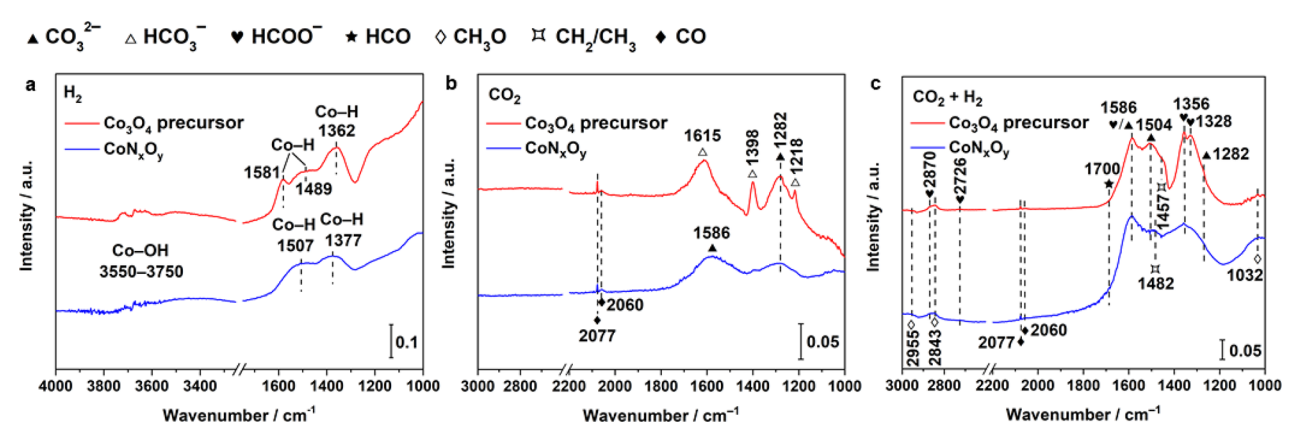


Figure 6. In situ DRIFTS measurements over the Co_3O_4 precursor and CoN_xO_y catalyst under the following conditions: (a) H_2 , (b) CO_2 , and (c) a H_2/CO_2 mixture at 240 °C for 1 h.

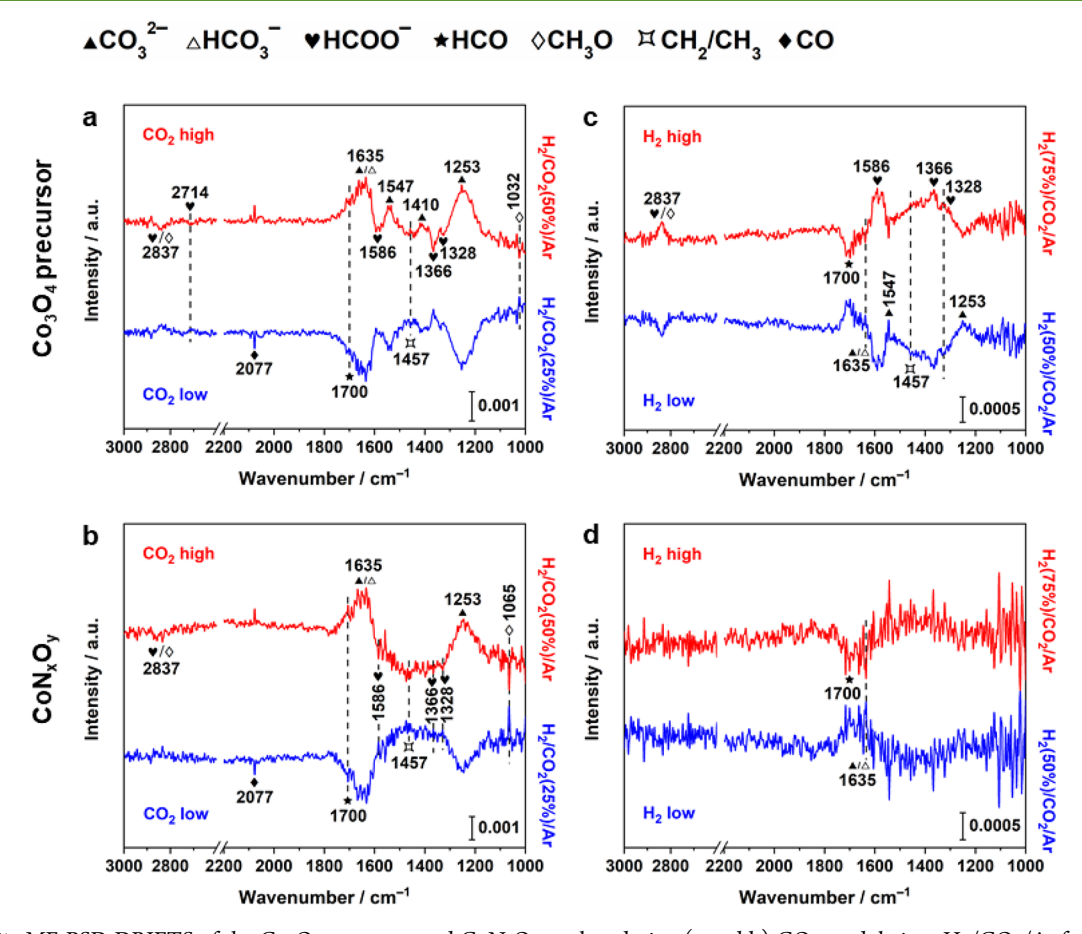


Figure 7. In situ ME-PSD-DRIFTS of the Co_3O_4 precursor and CoN_xO_y catalyst during (a and b) CO_2 modulation: $H_2/CO_2/Ar$ from $30/\underline{30}/0$ to $30/\underline{15}/15$ cm³ min⁻¹ and (c and d) H_2 modulation: $H_2/CO_2/Ar$ from $\underline{45}/15/0$ to $\underline{30}/15/15$ cm³ min⁻¹ under CO_2 hydrogenation conditions at 240 °C, with a total gas flow of 60 cm³ min⁻¹, and a modulation frequency of 1/90 Hz for the Co_3O_4 precursor (a and c) and CoN_xO_y (b and d) catalyst. Only the minimum and maximum CO_2 and H_2 spectra during modulation are shown for the sake of simplicity.

demonstrated more prominent desorption peaks centered at lower temperatures of 141 and 191 °C but a weakened one at 260 °C (Figure 5b). Such a shift to lower temperatures indicates that the strength of the basic sites in CoN_xO_y is weaker than that in the precursor. Overall, the weak and moderate strength basic sites (at ~140 and 200 °C) were approximately 1.6 times more significant in CoN_xO_y than in the Co_3O_4 precursor (see Table S7). The presence of weak and moderate basic sites, as indicated by the observations and catalytic results (Figure 3), plays a crucial role in regulating the

adsorption of CO_2 on the $\mathrm{CoN}_x\mathrm{O}_y$ catalyst. The enhanced oxygen vacancies and N doping ultimately promote the formation of C_{2+} hydrocarbons.

In situ DRIFTS was further conducted to illuminate the intermediate reaction species present during CO_2 hydrogenation on the Co_3O_4 precursor and the CoN_xO_y catalyst. First, H_2 was passed over the Co_3O_4 precursor and CoN_xO_y catalyst at 240 °C (Figure 6a). The peaks at approximately 3550–3750 cm⁻¹ for the Co_3O_4 precursor and CoN_xO_y catalyst suggested the appearance of a Co–OH group.

Scheme 1. Proposed Mechanistic Pathways for CO₂ Hydrogenation to CO, Methane, and Hydrocarbons over the Co₃O₄ Precursor and CoN_xO_y Catalyst^a

$$CO_{2(g)} \longrightarrow CO_{2(a)} \longrightarrow \forall HCOO_{(a)}^{-} \longrightarrow \forall HCO_{(a)} \longrightarrow$$

^aThe subscript (a) represents adsorbed species.

Furthermore, the generation of Co-H species at 1362, 1377, 1489, 1507, and 1581 cm⁻¹ evidenced H₂ activation on the Co₃O₄ precursor and CoN_xO_y catalyst. 46-49 Next, when Co₃O₄ and CoN_xO_y were contacted with only CO₂ at 240 °C (Figure 6b), characteristic bands for carbonate species (\(\blacktriangle \): 1282 and 1586 cm⁻¹) and bicarbonate species (\triangle : 1218, 1398, and 1615 cm⁻¹) were observed on the surface of Co₃O₄ (Table S8). 50-52 In contrast, the bands for bicarbonate species $(\triangle: 1218, 1398, \text{ and } 1615 \text{ cm}^{-1})$ were mostly absent on the CoN_xO_y catalyst, possibly due to the lower concentration of -OH on the CoN_xO_y catalyst. Weak peaks at 2060 and 2077 cm⁻¹ indicated that some CO₂ converted into linearly adsorbed CO species () on different Co sites. 50,52 In another parallel experiment, where the Co₃O₄ precursor and CoN_xO_y catalyst were contacted with a mixture of CO_2 and H_2 (Figure 6c), new peaks were observed in the stretching region of 2700-3000 cm⁻¹ for ν (CH) and 1000-1150 cm⁻¹ for $\nu(CO)$. These peaks were assigned to surface methoxy (\diamond : CH₃O)¹⁹ and formate (♥: HCOO)⁵¹ species (Tables S8 and S9, Figures S21 and S22). Additionally, peaks at 1457 and 1482 cm⁻¹, as well as 1700 cm⁻¹, were attributed to adsorbed CH_2/CH_3^{49} (\sharp) and formyl species (\star : HCO), respectively. More importantly, lower intensity and broadened characteristic peaks were generally observed on the CoN_xO_v catalyst (Figure 6a-c), implying weakly bonded intermediates or enhanced reactivity due to the surface modification by nitrogen atoms. The sharper IR features in Co₃O₄ suggest robust adsorption between the surface species and the catalyst surface. The stronger adsorption on the Co₃O₄ catalyst, higher surface site occupancy, and species overhydrogenation are all critical factors that contribute to the low activity and selectivity of the Co_3O_4 catalyst toward C_{2+} hydrocarbons.

These *in situ* DRIFTS experiments allowed us to identify possible intermediate species on the surface of the Co_3O_4 and CoN_xO_y catalysts under reaction conditions. However, multiple species (for example, intermediates and spectators) with various coverages and reactivities make it challenging to discriminate between the reaction intermediates and the

spectator species on the catalyst surface and understand their kinetic relevance. Therefore, we further performed ME-PSD-DRIFTS experiments, 50,53 a technique suitable for evaluating the dynamic response of surface species to periodic perturbations and assessing their kinetic response as possible reaction intermediate species.

The in situ ME-PSD-DRIFTS results for the Co₃O₄ precursor during the CO2 and H2 modulation are illustrated in Figure 7a,c, and Figure S23. In the case of CO₂ modulation (Figure 7a), several distinct peaks were observed on the Co₃O₄ precursor, including those assigned to (bi)carbonate (\triangle , \triangle : CO_3^{2-} , HCO_3^{-}), formate (\heartsuit : HCOO), formyl (\bigstar : HCO), CO (\spadesuit) , and slightly discernible CH_2/CH_3 (\sharp) and methoxy (\diamondsuit : CH₃O) species. The signal intensity of (bi)carbonate $(\triangle, \blacktriangle)$, formyl $(\bigstar: HCO)$, and $CO(\spadesuit)$ species increased, whereas that of formate (\P) , methoxy $(\diamondsuit: CH_3O)$, and $CH_2/$ CH_3 (Ξ) species decreased as the CO_2 concentration increased (Figure 7a,b). This phenomenon is attributed to the lower concentration of Co-H species (i.e., lower H_2/CO_2) on the catalyst surface, indicating that the RWGS reaction primarily proceeds via a carbonate route under these reaction conditions. On the other hand, at lower CO_2 concentrations (i.e., high H_2 / CO₂), CO₂ hydrogenation via a formate route toward hydrocarbons appears more likely. Therefore, based on the reactivity studies and in situ ME-PSD-DRIFTS results, we propose that the observed surface (bi)carbonate, formate, formyl, CO, methoxy, and CH₂/CH₃ species are likely reaction intermediates on the Co₃O₄ precursor. More specifically, (bi)carbonate species were seen to dominate the formation of CO at low H₂/CO₂ ratios, whereas formate species appeared to be the primary species for C₂₊ hydrocarbon production at high H₂/CO₂ ratios. The spectra for the CoN_xO_y catalyst (Figure 7b) showed features similar to those observed for the Co₃O₄ precursor under identical modulation conditions but with reduced intensity, suggesting similar reaction pathways. However, one of the most evident differences was the absence of the (as)symmetric vibration of unidentate carbonate (\triangle : 1410 and 1547 cm⁻¹), 54 which proved that nitridation changed

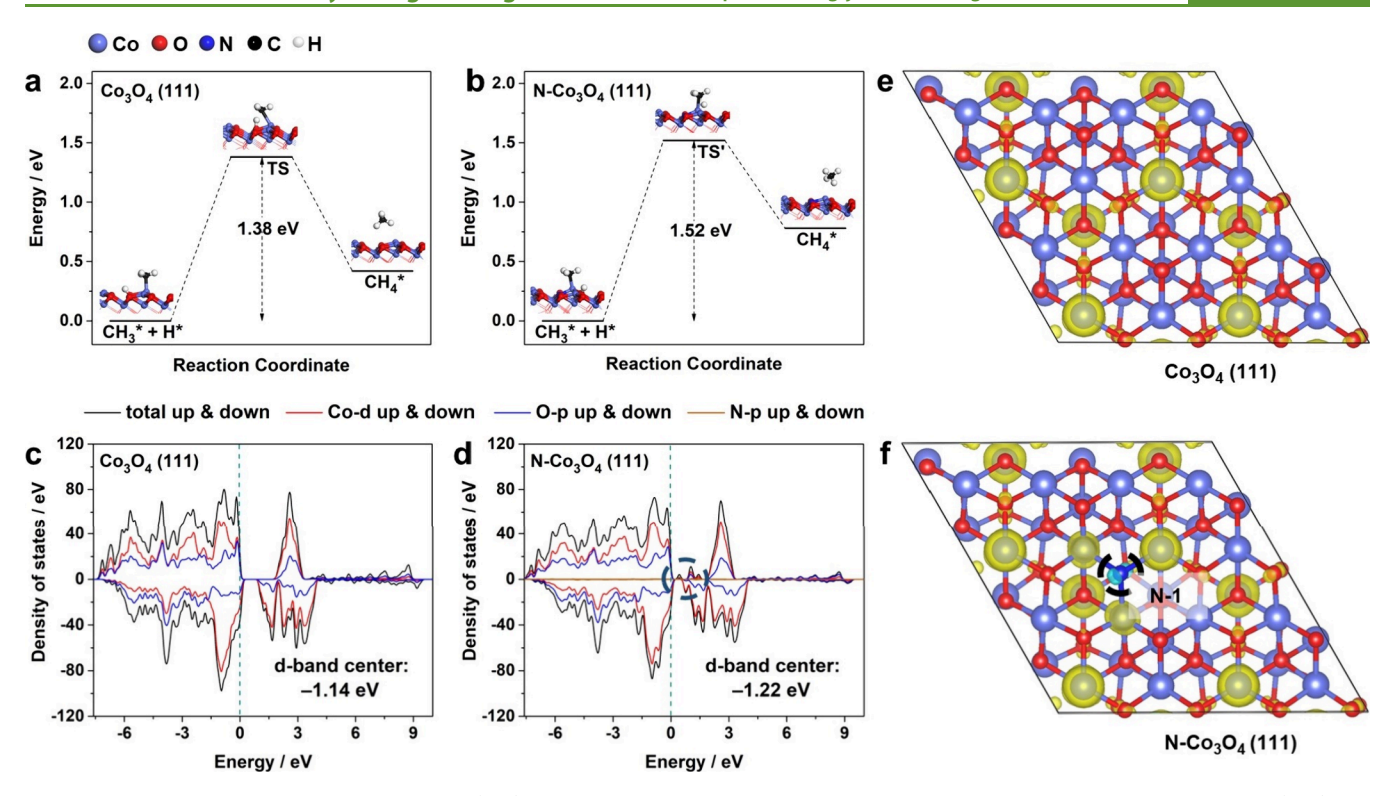


Figure 8. Density-functional theory calculations. (a, b) Potential energy for CH_4^* formation from CH_3^* and H^* coadsorption on Co_3O_4 (111) and $N-Co_3O_4$ (111) surfaces. The coadsorption energies of CH_3^* and H^* on the Co_3O_4 (111) or $N-Co_3O_4$ (111) surfaces are considered to be zero. TS and TS' correspond to the transition states for Co_3O_4 (111) and $N-Co_3O_4$ (111) surfaces, respectively. The insets in panels a and b show the side views of the DFT-optimized adsorption geometries of the initial, transition, and final states in the hydrogenation of $CH_3^* + H^*$ on the Co_3O_4 (111) and $N-Co_3O_4$ (111) surfaces. (c, d) Total and partial electronic density of states for Co_3O_4 (111) and $N-Co_3O_4$ (111). (e, f) Top views of the spin density of Co_3O_4 (111) and $N-Co_3O_4$ (111) surfaces. The yellow circles are the spin density on the Co_3O_4 (111) and white colors, respectively.

the adsorption state of the carbonate species (Figure 7b). This phenomenon indicates a more active catalytic surface of the CoN_xO_v catalyst.

The H₂ modulation for the Co₃O₄ precursor (Figure 7c and Figure S24) resulted in opposite changes to the CO₂ modulation, as seen in the similarity between the spectra at low CO₂ concentration in Figure 7a and high H₂ concentration in Figure 7c. Both conditions led to high H₂/CO₂ reaction conditions. Additionally, Figure 7c shows that the signals for formate (♥; 1328, 1366, and 1586 cm⁻¹) and CH₂/CH₃ species (II; 1457 cm⁻¹) increased at high H₂ concentration, suggesting a positive H2 reaction rate order. This finding is also supported by the results shown in Figure 4a. From the DRIFTS spectra, it is speculated that the conversion of the formate species is slow (Figure S25). Meanwhile, formyl species, generally considered to be the hydrogenation products of adsorbed formate species, displayed lower intensity due to their relatively higher reactivity. Therefore, we propose that the conversion of formate species is the rate-determining step, whereas carbonate species appear to control the formation of CO via the RWGS reaction. In the case of the CoN_xO_y catalyst during H₂ modulation (Figure 7d), the signals of adsorbed species are significantly reduced, even more than those during CO₂ modulation (Figure 7b). This phenomenon indicates that the N-doped surface is more reactive and effective for hydrogenation reactions than the surface of the Co₃O₄ precursor. We also conducted reaction tests of CH₄, CH₃OH, and C₂H₅OH with the CoN_xO_y catalyst at 240 $^{\circ}$ C,

respectively. The results (Figures S26–S28 and Table S10) proved that CO_2 hydrogenation did not primarily proceed via methane coupling, MTO process, or C_2H_5OH conversion.

Based on the above experiments, we propose a probable reaction mechanism (Scheme 1) for the hydrogenation of CO_2 to CO, methane, and hydrocarbons over the Co_3O_4 precursor and CoN_xO_y catalyst. Three primary pathways can be distinguished: (A) RWGS for CO formation via carbonate species (\spadesuit), CO species (\spadesuit), and/or formate species (\P); (B) methanation via CO species (\spadesuit) and/or formate species (\P); and (C) chain growth to C_{2+} hydrocarbons via formate species (\P).

Density-Functional Theory (DFT) Calculations. DFT calculations were performed to gain insights into the catalytic activity and selectivity differences between the parent Co₃O₄ precursor and the CoN_xO_y catalyst. The calculation model was constructed based on two reasons. First, the in situ XPS results of the CoN_rO_v catalyst demonstrate that no significant changes in the oxidation state of Co 2p were observed (Figure S29), indicating that Co2+ is likely the active species during CO2 hydrogenation and that the active site structures are similar to those of the fresh catalyst. Second, the Co₃O₄ (111) crystal plane (Figure S30 and Table S11) was the primary plane observed in the TEM image (Figure 1e). Therefore, the Co₃O₄ (111) crystal plane was selected as the computational model for the calculations. This lattice plane was subsequently modified to create the computational model for a N-doped Co_3O_4 catalyst (CoN_xO_y) , which was generated by replacing

an O atom in the Co₃O₄ (111) crystal plane with a N atom (Figure S31). The developed structural model matched well with the results obtained from ToF-SIMS (Figure 2d). For simplicity, the formation of CH₄ and a C-C coupling product (C₂H₄) was explored to investigate possible selectivity differences on the various surfaces. As a first step in the calculations, the activation energy barriers (E_a) for CH_4 formation $(CH_3^* + H^* \rightarrow CH_4^*)$ were calculated on Co_3O_4 (111) and N-Co₃O₄ (111) surfaces (Figure 8a,b). According to the calculation results for the different possible combinations of adsorption sites for the intermediate species (Table S12), it was found that H is more favorably bound to the Co₃O₄ (111) surface via an O_a (an O linked to one Co²⁺ and two Co³⁺), whereas CH₃ is attached to Co²⁺. The calculations also indicated that the reaction energy for CH4 formation on the Co₃O₄ (111) surface was endothermic by 0.42 eV, whereas the energy barrier E_a was 1.38 eV. The possible $CH_3^* + H^*$ coadsorption configurations on the N-Co₃O₄ (111) surface were optimized, and they were the same as in the case of Co₃O₄ (111) (Figure S32). In contrast, this reaction was found to be more endothermic (0.78 eV) and less favorable (E_a = 1.52 eV) on the N-Co₃O₄ (111) surface, indicating that methane formation is less favorable on the $N-Co_3O_4$ (111) surface when compared to the Co_3O_4 (111) surface. Following these calculations, we also determined the activation energy barriers (E_a) for $C_2H_4^*$ formation $(CH_2^* + CH_2^* \rightarrow C_2H_4^*)$ on the Co_3O_4 (111) and N- Co_3O_4 (111) surfaces, which were found to be 0.83 and 0.74 eV, respectively (Figure S33). These results offer further theoretical support for the enhanced hydrogenation of CO_2 to C_{2+} hydrocarbons on the CoN_xO_y surface and are consistent with the increased C2+ selectivity on the CoN_xO_v catalyst compared to the Co_3O_4 precursor (Figure

The densities of states (DOS) for Co₂O₄ (111) and N-Co₃O₄ (111) were determined and used to gain a more indepth understanding of the differences in the electronic states of both surfaces. The calculated DOS results indicated that new energy levels were introduced near the Fermi level after nitrogen doping of Co₃O₄ (111). These levels were attributed to contributions from the spin-up of N 2p, O 2p, and Co 3d, as well as the spin-down of O 2p and Co 3d (Figure 8c,d and Figure S34). The band gap in N-Co₃O₄ (111) was narrower than that of Co₃O₄ (111), making electron transfer more accessible and reducing the activation energy for CO₂. Additionally, the increase in the spin density on the N-Co₃O₄ (111) surface compared to that on the Co₃O₄ (111) surface indicated a higher concentration of Co2+ after nitridation (Figure 8e,f), which was also beneficial for CO₂ activation. These conclusions are also supported by the results obtained from XPS and XANES (Figure 2a and Figure S4). Additionally, the d-band center (ε_d) for the N-Co₃O₄ (111) surface (-1.22 eV) shifted downward from the Fermi level (Figure S35) in comparison to that of the Co₃O₄ (111) surface (-1.14 eV), resulting in a decreased antibonding energy state. As a result, the adsorption energy of the reaction intermediates decreased, 55,56 which in turn facilitated the formation of C_{2+} hydrocarbons instead of CH₄ on the N-doped Co₃O₄ material.

CONCLUSIONS

We successfully synthesized a mesoporous CoN_xO_y catalyst with a relatively large surface area (approximately 90 m² g⁻¹), which exhibited an enhanced CO_2 conversion (25%) and C_{2+} hydrocarbon selectivity (42 C-mol%) when compared to the

undoped parent Co₃O₄ (9% and 3 C-mol%, respectively). The CoN_xO_y catalyst possessed higher adsorption and activation sites for CO2, higher energy barrier for CH4 formation, and weakened adsorption of reaction intermediates, thereby enhancing CO₂ conversion and C₂₊ product selectivity. In situ DRIFTS during H2, CO2, and H2/CO2 exposure and in situ ME-PSD-DRIFTS during H₂ and CO₂ concentration modulation at the reaction temperature showed that H₂ was activated to generate Co-H species and Co-OH groups. In contrast, CO₂ was activated mainly to form carbonate, bicarbonate, and formate species. A catalytic reaction process is proposed where (1) CO₂ is converted to CO through the RWGS via a carbonate pathway and (2) CO₂ is converted to C₂₊ hydrocarbons mainly through C-C coupling of CH_z surface species derived from hydrodeoxygenated formate species (Scheme 1). Our experimental results demonstrate that transition metal nitrides can be alternative materials for controlling the product distribution in CO₂ hydrogenation by varying the electronic state of the catalyst. We expect our findings to inspire new ideas for synthesizing the next generation of catalysts for the hydrogenation of CO2 to higher hydrocarbons.

ASSOCIATED CONTENT

Supporting Information

The Supporting Information is available free of charge at https://pubs.acs.org/doi/10.1021/acssuschemeng.3c07908.

Part of the experimental section, SEM, XPS, *in situ* XPS, N₂ physisorption, physicochemical properties, XANES, GC, GC/MS, ¹H NMR, catalytic performance, Aspen simulation, *in situ* DRIFTS, *in situ* ME-PSD-DRIFTS, and DFT results (PDF)

AUTHOR INFORMATION

Corresponding Authors

Guiru Wang - College of Energy and Materials Engineering, Taiyuan University of Science and Technology, Taiyuan 030024, P.R. China; Email: wangguiru@tyust.edu.cn

Juan J. Bravo-Suárez — Center for Environmentally Beneficial Catalysis, The University of Kansas, Lawrence, Kansas 66047, United States; Department of Chemical and Petroleum Engineering, The University of Kansas, Lawrence, Kansas 66045, United States; orcid.org/0000-0002-6484-374X; Email: jjbravo@ku.edu

Jian-Feng Wu — State Key Laboratory of Applied Organic Chemistry, Key Laboratory of Nonferrous Metals Chemistry and Resources Utilization of Gansu Province, College of Chemistry and Chemical Engineering, Lanzhou University, Lanzhou 730000, P.R. China; State Key Laboratory for Oxo Synthesis and Selective Oxidation, Lanzhou Institute of Chemical Physics, Chinese Academy of Sciences, Lanzhou, Gansu 730000, P.R. China; orcid.org/0000-0003-4444-2639; Email: wjf@licp.cas.cn

Authors

Ming-Ming Yu — State Key Laboratory of Applied Organic Chemistry, Key Laboratory of Nonferrous Metals Chemistry and Resources Utilization of Gansu Province, College of Chemistry and Chemical Engineering, Lanzhou University, Lanzhou 730000, P.R. China

Zhenghao Zhang — State Key Laboratory of Applied Organic Chemistry, Key Laboratory of Nonferrous Metals Chemistry

- and Resources Utilization of Gansu Province, College of Chemistry and Chemical Engineering, Lanzhou University, Lanzhou 730000, P.R. China
- Gui-Ling Guan State Key Laboratory of Applied Organic Chemistry, Key Laboratory of Nonferrous Metals Chemistry and Resources Utilization of Gansu Province, College of Chemistry and Chemical Engineering, Lanzhou University, Lanzhou 730000, P.R. China; State Key Laboratory for Oxo Synthesis and Selective Oxidation, Lanzhou Institute of Chemical Physics, Chinese Academy of Sciences, Lanzhou, Gansu 730000, P.R. China
- Bhagyesha Patil Center for Environmentally Beneficial Catalysis, The University of Kansas, Lawrence, Kansas 66047, United States; Department of Chemical and Petroleum Engineering, The University of Kansas, Lawrence, Kansas 66045, United States
- Priya Darshini Srinivasan Center for Environmentally Beneficial Catalysis, The University of Kansas, Lawrence, Kansas 66047, United States; Department of Chemical and Petroleum Engineering, The University of Kansas, Lawrence, Kansas 66045, United States
- Wen-Hua Feng State Key Laboratory of Applied Organic Chemistry, Key Laboratory of Nonferrous Metals Chemistry and Resources Utilization of Gansu Province, College of Chemistry and Chemical Engineering, Lanzhou University, Lanzhou 730000, P.R. China
- Yu-Ting Miao State Key Laboratory of Applied Organic Chemistry, Key Laboratory of Nonferrous Metals Chemistry and Resources Utilization of Gansu Province, College of Chemistry and Chemical Engineering, Lanzhou University, Lanzhou 730000, P.R. China
- Li-Jun Wang State Key Laboratory of Applied Organic Chemistry, Key Laboratory of Nonferrous Metals Chemistry and Resources Utilization of Gansu Province, College of Chemistry and Chemical Engineering, Lanzhou University, Lanzhou 730000, P.R. China
- Hongda Zhu Center for Environmentally Beneficial Catalysis, The University of Kansas, Lawrence, Kansas 66047, United States; Department of Chemical and Petroleum Engineering, The University of Kansas, Lawrence, Kansas 66045, United States
- **Mohsen Shakouri** Canadian Light Source, Saskatoon, Saskatchewan S7N 2 V3, Canada
- Rong Huang Vacuum Interconnected Nanotech Workstation, Suzhou Institute of Nano-Tech and Nano-Bionics, Chinese Academy of Sciences (CAS), Suzhou 215123, P.R. China
- Ding Ding Vacuum Interconnected Nanotech Workstation, Suzhou Institute of Nano-Tech and Nano-Bionics, Chinese Academy of Sciences (CAS), Suzhou 215123, P.R. China
- Wenwu Sun Thermo Fisher Scientific (China) Co., Ltd., Shanghai 201206, P.R. China
- Yongfeng Hu − Canadian Light Source, Saskatoon, Saskatchewan S7N 2 V3, Canada; oorcid.org/0000-0002-7510-9444
- Si-Min Yu State Key Laboratory of Applied Organic Chemistry, Key Laboratory of Nonferrous Metals Chemistry and Resources Utilization of Gansu Province, College of Chemistry and Chemical Engineering, Lanzhou University, Lanzhou 730000, P.R. China
- Yi Cui Vacuum Interconnected Nanotech Workstation, Suzhou Institute of Nano-Tech and Nano-Bionics, Chinese

- Academy of Sciences (CAS), Suzhou 215123, P.R. China; orcid.org/0000-0002-9182-9038
- Qiang Wang State Key Laboratory of Coal Conversion, Institute of Coal Chemistry, Chinese Academy of Sciences, Taiyuan 030001, P.R. China; orcid.org/0000-0001-7301-9341
- Jin-Hui Yang State Key Laboratory of High-efficiency Utilization of Coal and Green Chemical Engineering, College of Chemistry and Chemical Engineering, Ningxia University, Yinchuan 750021, P.R. China
- Lingjun Chou State Key Laboratory for Oxo Synthesis and Selective Oxidation, Lanzhou Institute of Chemical Physics, Chinese Academy of Sciences, Lanzhou, Gansu 730000, P.R. China; orcid.org/0000-0002-1888-7506

Complete contact information is available at: https://pubs.acs.org/10.1021/acssuschemeng.3c07908

Author Contributions

[&]M.-M.Y., Z.Z., and G.-L.G. contributed equally to this work. **Notes**

The authors declare no competing financial interest.

ACKNOWLEDGMENTS

This project was financially supported by the National Natural Science Foundation of China (nos. 21903041 and 21803027), the Key Talent Project of Gansu Province, Fundamental Research Funds for the Central Universities (lzujbky-2021ey11), and Foundation of State Key Laboratory of Highefficiency Utilization of Coal and Green Chemical Engineering (grant 2022-K07). J.J.B.-S. acknowledges the financial support from the National Science Foundation under grant CBET-1847655. Q.W. acknowledges the financial support from the Joint Fund of Yulin University and the Dalian National Laboratory for Clean Energy (no. 2021006). We thank the Electron Microscopy Centre of Lanzhou University for the microscopy and microanalysis of our specimens and the technical support for Nano-X from the Suzhou Institute of Nano-Tech and Nano-Bionics, Chinese Academy of Sciences (SINANO). We thank the Canadian Light Source for the XANES measurement at the SXRMB beamline. We thank Prof. Huahua Zhao (Lanzhou Institute of Chemical Physics), Fangling Yang (Lanzhou University), Prof. Panpan Zhou (Lanzhou University), Yantao Wang (Lanzhou University), and Dr. Xiaozhi Su (Shanghai Synchrotron Radiation Facility) for helpful discussions.

■ REFERENCES

- (1) Sakakura, T.; Choi, J.-C.; Yasuda, H. Transformation of carbon dioxide. *Chem. Rev.* **2007**, *107*, 2365–2387.
- (2) Wang, W.; Wang, S.; Ma, X.; Gong, J. Recent advances in catalytic hydrogenation of carbon dioxide. *Chem. Soc. Rev.* **2011**, *40*, 3703–27.
- (3) Olah, G. A.; Prakash, G. K. S.; Goeppert, A. Anthropogenic chemical carbon cycle for a sustainable future. *J. Am. Chem. Soc.* **2011**, 133, 12881–12898.
- (4) He, M.; Sun, Y.; Han, B. Green carbon science: scientific basis for integrating carbon resource processing, utilization, and recycling. *Angew. Chem., Int. Ed.* **2013**, 52, 9620–9633.
- (5) Alvarez, A.; Bansode, A.; Urakawa, A.; Bavykina, A. V.; Wezendonk, T. A.; Makkee, M.; Gascon, J.; Kapteijn, F. Challenges in the greener production of formates/formic acid, methanol, and DME by heterogeneously catalyzed CO₂ hydrogenation processes. *Chem. Rev.* **2017**, *117*, 9804–9838.

- (6) Zhou, W.; Cheng, K.; Kang, J.; Zhou, C.; Subramanian, V.; Zhang, Q.; Wang, Y. New horizon in C1 chemistry: breaking the selectivity limitation in transformation of syngas and hydrogenation of CO₂ into hydrocarbon chemicals and fuels. *Chem. Soc. Rev.* **2019**, *48*, 3193–3228.
- (7) Shang, X.; Liu, G.; Su, X.; Huang, Y.; Zhang, T. A review of the recent progress on direct heterogeneous catalytic CO₂ hydrogenation to gasoline-range hydrocarbons. *EES Catal.* **2023**, *1*, 353–368.
- (8) Marques Mota, F.; Kim, D. H. From CO₂ methanation to ambitious long-chain hydrocarbons: alternative fuels paving the path to sustainability. *Chem. Soc. Rev.* **2019**, *48*, 205–259.
- (9) Zhang, S.; Wu, Z.; Liu, X.; Shao, Z.; Xia, L.; Zhong, L.; Wang, H.; Sun, Y. Tuning the interaction between Na and Co₂C to promote selective CO₂ hydrogenation to ethanol. *Appl. Catal.*, B **2021**, 293, No. 120207.
- (10) Have, I. C. t.; Kromwijk, J. J. G.; Monai, M.; Ferri, D.; Sterk, E. B.; Meirer, F.; Weckhuysen, B. M. Uncovering the reaction mechanism behind CoO as active phase for CO₂ hydrogenation. *Nat. Commun.* **2022**, *13*, 324.
- (11) Li, B.; Ma, B.; Wang, S.-Y.; Yu, M.-M.; Zhang, Z.-Q.; Xiao, M.-J.; Zhang, H.; Wu, J.-F.; Peng, Y.; Wang, Q.; Zhang, H.-L. Vacancy engineering of two-dimensional W₂N₃ nanosheets for efficient CO₂ hydrogenation. *Nanoscale* **2022**, *14*, 9736–9742.
- (12) de Smit, E.; Weckhuysen, B. M. The renaissance of iron-based Fischer—Tropsch synthesis: on the multifaceted catalyst deactivation behaviour. *Chem. Soc. Rev.* **2008**, *37*, 2758–2781.
- (13) Rahmati, M.; Safdari, M.-S.; Fletcher, T. H.; Argyle, M. D.; Bartholomew, C. H. Chemical and thermal sintering of supported metals with emphasis on cobalt catalysts during Fischer—Tropsch synthesis. *Chem. Rev.* **2020**, *120*, 4455–4533.
- (14) Zhai, P.; Li, Y.; Wang, M.; Liu, J.; Cao, Z.; Zhang, J.; Xu, Y.; Liu, X.; Li, Y.-W.; Zhu, Q.; Xiao, D.; Wen, X.-D.; Ma, D. Development of direct conversion of syngas to unsaturated hydrocarbons based on Fischer–Tropsch route. *Chem.* **2021**, *7*, 3027–3051
- (15) Chen, Y.; Wei, J.; Duyar, M. S.; Ordomsky, V. V.; Khodakov, A. Y.; Liu, J. Carbon-based catalysts for Fischer–Tropsch synthesis. *Chem. Soc. Rev.* **2021**, *50*, 2337–2366.
- (16) Munnik, P.; de Jongh, P. E.; de Jong, K. P. Control and impact of the nanoscale distribution of supported cobalt particles used in Fischer–Tropsch catalysis. *J. Am. Chem. Soc.* **2014**, *136*, 7333–7340.
- (17) Zhong, L.; Yu, F.; An, Y.; Zhao, Y.; Sun, Y.; Li, Z.; Lin, T.; Lin, Y.; Qi, X.; Dai, Y.; Gu, L.; Hu, J.; Jin, S.; Shen, Q.; Wang, H. Cobalt carbide nanoprisms for direct production of lower olefins from syngas. *Nature* **2016**, *538*, 84–87.
- (18) Li, J.; He, Y.; Tan, L.; Zhang, P.; Peng, X.; Oruganti, A.; Yang, G.; Abe, H.; Wang, Y.; Tsubaki, N. Integrated tuneable synthesis of liquid fuels via Fischer—Tropsch technology. *Nat. Catal.* **2018**, *1*, 787–793.
- (19) Wang, L.; Guan, E.; Wang, Y.; Wang, L.; Gong, Z.; Cui, Y.; Meng, X.; Gates, B. C.; Xiao, F.-S. Silica accelerates the selective hydrogenation of CO_2 to methanol on cobalt catalysts. *Nat. Commun.* **2020**, *11*, 1033.
- (20) Zhai, P.; Xu, C.; Gao, R.; Liu, X.; Li, M.; Li, W.; Fu, X.; Jia, C.; Xie, J.; Zhao, M.; Wang, X.; Li, Y.-W.; Zhang, Q.; Wen, X.-D.; Ma, D. Highly tunable selectivity for syngas-derived alkenes over zinc and sodium-modulated Fe₅C₂ Catalyst. *Angew. Chem., Int. Ed.* **2016**, 55, 9902–9907.
- (21) Wei, J.; Ge, Q.; Yao, R.; Wen, Z.; Fang, C.; Guo, L.; Xu, H.; Sun, J. Directly converting CO_2 into a gasoline fuel. *Nat. Commun.* **2017**, *8*, 15174–15182.
- (22) Prieto, G. Carbon dioxide hydrogenation into higher hydrocarbons and oxygenates: thermodynamic and kinetic bounds and progress with heterogeneous and homogeneous catalysis. *ChemSusChem* **2017**, *10*, 1056–1070.
- (23) Jimenez, J. D.; Wen, C.; Royko, M. M.; Kropf, A. J.; Segre, C.; Lauterbach, J. Influence of coordination environment of anchored single-site cobalt catalyst on CO₂ hydrogenation. *ChemCatChem* **2020**, *12*, 846–854.

- (24) Vrijburg, W. L.; Moioli, E.; Chen, W.; Zhang, M.; Terlingen, B. J. P.; Zijlstra, B.; Filot, I. A. W.; Züttel, A.; Pidko, E. A.; Hensen, E. J. M. Efficient base-metal NiMn/TiO₂ catalyst for CO₂ methanation. *ACS Catal.* **2019**, *9*, 7823–7839.
- (25) Zhong, Y.; Xia, X.; Shi, F.; Zhan, J.; Tu, J.; Fan, H. J. Transition metal carbides and nitrides in energy storage and conversion. *Adv. Sci.* **2016**, *3*, 1500286.
- (26) Lin, T.; Qi, X.; Wang, X.; Xia, L.; Wang, C.; Yu, F.; Wang, H.; Li, S.; Zhong, L.; Sun, Y. Direct production of higher oxygenates by syngas conversion over a multifunctional catalyst. *Angew. Chem., Int. Ed.* **2019**, *58*, 4627–4631.
- (27) Zhang, S.; Liu, X.; Shao, Z.; Wang, H.; Sun, Y. Direct $\rm CO_2$ hydrogenation to ethanol over supported $\rm Co_2C$ catalysts: studies on support effects and mechanism. *J. Catal.* **2020**, 382, 86–96.
- (28) Wang, L.; Zhang, W.; Zheng, X.; Chen, Y.; Wu, W.; Qiu, J.; Zhao, X.; Zhao, X.; Dai, Y.; Zeng, J. Incorporating nitrogen atoms into cobalt nanosheets as a strategy to boost catalytic activity toward $\rm CO_2$ hydrogenation. *Nat. Energy* **2017**, *2*, 869–876.
- (29) Abou Hamdan, M.; Nassereddine, A.; Checa, R.; Jahjah, M.; Pinel, C.; Piccolo, L.; Perret, N. Supported molybdenum carbide and nitride catalysts for carbon dioxide hydrogenation. *Front. Chem.* **2020**, *8*, 452.
- (30) Zhao, B.; Sun, M.; Chen, F.; Shi, Y.; Yu, Y.; Li, X.; Zhang, B. Unveiling the activity origin of iron nitride as catalytic material for efficient hydrogenation of CO_2 to C_{2+} Hydrocarbons. *Angew. Chem., Int. Ed.* **2021**, *60*, 4496–4500.
- (31) Shi, Y.; Wan, Y.; Zhang, R.; Zhao, D. Synthesis of self-supported ordered mesoporous cobalt and chromium nitrides. *Adv. Funct. Mater.* **2008**, *18*, 2436–2443.
- (32) Dudarev, S. L.; Botton, G. A.; Savrasov, S. Y.; Humphreys, C. J.; Sutton, A. P. Electron-energy-loss spectra and the structural stability of nickel oxide: An LSDA+U study. *Phys. Rev. B* **1998**, *57*, 1505–1509
- (33) Kruk, M.; Jaroniec, M. Gas adsorption characterization of ordered organic–inorganic nanocomposite materials. *Chem. Mater.* **2001**, *13*, 3169–3183.
- (34) Biesinger, M. C.; Payne, B. P.; Grosvenor, A. P.; Lau, L. W. M.; Gerson, A. R.; Smart, R. S. C. Resolving surface chemical states in XPS analysis of first row transition metals, oxides and hydroxides: Cr, Mn, Fe. *Co and Ni. Appl. Surf. Sci.* **2011**, 257, 2717–2730.
- (35) https://www.thermofisher.cn/cn/zh/home/industrial/spectroscopy-elemental-isotope-analysis/surface-analysis/xpssimplified/periodic-table/cobalt.html (accessed 2023–11–29).
- (36) Wang, L.; Zhang, S.; Zhu, Y.; Patlolla, A.; Shan, J.; Yoshida, H.; Takeda, S.; Frenkel, A. I.; Tao, F. Catalysis and in situ studies of Rh₁/Co₃O₄ nanorods in reduction of NO with H₂. ACS Catal. **2013**, 3, 1011–1019.
- (37) Razzaq, R.; Li, C.; Usman, M.; Suzuki, K.; Zhang, S. A highly active and stable $\text{Co}_4\text{N}/\gamma\text{-}\text{Al}_2\text{O}_3$ catalyst for CO and CO₂ methanation to produce synthetic natural gas (SNG). *Chem. Eng. J.* 2015, 262, 1090–1098.
- (38) https://www.thermofisher.cn/cn/zh/home/industrial/spectroscopy-elemental-isotope-analysis/surface-analysis/xpssimplified/periodic-table/nitrogen.html (accessed 2023–11–29).
- (39) https://www.thermofisher.cn/cn/zh/home/industrial/spectroscopy-elemental-isotope-analysis/surface-analysis/xpssimplified/periodic-table/oxygen.html (accessed 2023–11–29).
- (40) Grams, J. Surface studies of heterogeneous catalysts by time-of-flight secondary ion mass spectrometry. *Eur. J. Mass Spectrom.* **2010**, 16, 453–461.
- (41) Hofmann, J. P.; Rohnke, M.; Weckhuysen, B. M. Recent advances in secondary ion mass spectrometry of solid acid catalysts: large zeolite crystals under bombardment. *Phys. Chem. Chem. Phys.* **2014**, *16*, 5465–5474.
- (42) Feng, W.-H.; Yu, M.-M.; Wang, L.-J.; Miao, Y.-T.; Shakouri, M.; Ran, J.; Hu, Y.; Li, Z.; Huang, R.; Lu, Y.-L.; Gao, D.; Wu, J.-F. Insights into bimetallic oxide synergy during carbon dioxide hydrogenation to methanol and dimethyl ether over $GaZrO_x$ oxide catalysts. *ACS Catal.* **2021**, *11*, 4704–4711.

- (43) Wang, C.-W.; Sun, Y.; Wang, L.-J.; Feng, W.-H.; Miao, Y.-T.; Yu, M.-M.; Wang, Y.-X.; Gao, X.-D.; Zhao, Q.; Ding, Z.; Feng, Z.; Yu, S.-M.; Yang, J.; Hu, Y.; Wu, J.-F. Oxidative carbonylation of methane to acetic acid on an Fe-modified ZSM-5 zeolite. *Appl. Catal., B* **2023**, 329, No. 122549.
- (44) Yu, Q.; Liu, C.; Li, X.; Wang, C.; Wang, X.; Cao, H.; Zhao, M.; Wu, G.; Su, W.; Ma, T.; Zhang, J.; Bao, H.; Wang, J.; Ding, B.; He, M.; Yamauchi, Y.; Zhao, X. S. N-doping activated defective Co_3O_4 as an efficient catalyst for low-temperature methane oxidation. *Appl. Catal., B* **2020**, 269, No. 118757.
- (45) Zecchina, A.; Spoto, G. Spectroscopic study of the interaction of H₂ with MgO-CoO solid solutions. *Z. Phys. Chem.* **1983**, *137*, 173–185.
- (46) Collins, S. E.; Baltanás, M. A.; Bonivardi, A. L. An infrared study of the intermediates of methanol synthesis from carbon dioxide over Pd/ β -Ga₂O₃. *J. Catal.* **2004**, 226, 410–421.
- (47) Copéret, C.; Estes, D. P.; Larmier, K.; Searles, K. Isolated surface hydrides: formation, structure, and reactivity. *Chem. Rev.* **2016**, *116*, 8463–8505.
- (48) Wang, J.; Li, G.; Li, Z.; Tang, C.; Feng, Z.; An, H.; Liu, H.; Liu, T.; Li, C. A highly selective and stable ZnO-ZrO₂ solid solution catalyst for CO₂ hydrogenation to methanol. *Sci. Adv.* **2017**, 3, No. e1701290.
- (49) He, Z.; Cui, M.; Qian, Q.; Zhang, J.; Liu, H.; Han, B. Synthesis of liquid fuel via direct hydrogenation of CO₂. *Proc. Natl. Acad. Sci. U.S.A.* **2019**, *116*, 12654–12659.
- (50) Kumar, N.; Jothimurugesan, K.; Stanley, G. G.; Schwartz, V.; Spivey, J. J. In situ FT-IR study on the effect of cobalt precursors on CO adsorption behavior. *J. Phys. Chem. C* **2011**, *115*, 990–998.
- (51) Wang, L.; He, S.; Wang, L.; Lei, Y.; Meng, X.; Xiao, F.-S. Cobalt—nickel catalysts for selective hydrogenation of carbon dioxide into ethanol. *ACS Catal.* **2019**, *9*, 11335—11340.
- (52) Liu, R.; Leshchev, D.; Stavitski, E.; Juneau, M.; Agwara, J. N.; Porosoff, M. D. Selective hydrogenation of CO₂ and CO over potassium promoted Co/ZSM-5. *Appl. Catal., B* **2021**, 284, No. 119787.
- (53) Patil, B. S.; Srinivasan, P. D.; Atchison, E.; Zhu, H.; Bravo-Suárez, J. J. Design, modelling, and application of a low void-volume in situ diffuse reflectance spectroscopic reaction cell for transient catalytic studies. *React. Chem. Eng.* **2019**, *4*, 667–678.
- (54) Coenen, K.; Gallucci, F.; Mezari, B.; Hensen, E.; van Sint Annaland, M. An in-situ IR study on the adsorption of CO₂ and H₂O on hydrotalcites. *J. CO2 Util.* **2018**, 24, 228–239.
- (55) Hammer, B.; Norskov, J. K. Why gold is the noblest of all the metals. *Nature* **1995**, *376*, 238–240.
- (56) Chen, Z.; Song, Y.; Cai, J.; Zheng, X.; Han, D.; Wu, Y.; Zang, Y.; Niu, S.; Liu, Y.; Zhu, J.; Liu, X.; Wang, G. Tailoring the d-band centers enables Co_4N nanosheets to be highly active for hydrogen evolution catalysis. *Angew. Chem., Int. Ed.* **2018**, *57*, 5076–5080.